Attenuation correction for whole-body PET imaging using automated fuzzy clustering-based segmentation method

Habib Zaidi, *Member, IEEE,* Manuel Diaz-Gomez, Abdelouahab Boudraa, Daniel O Slosman

Abstract-- **Segmented-based attenuation correction is now a widely accepted technique to reduce noise contribution of measured attenuation correction. In this paper, we present a new method for segmenting transmission images in positron emission tomography. This reduces the noise on the correction maps while still correcting for differing attenuation coefficients of specific tissues. Based on the Fuzzy C-Means (FCM) algorithm, the method segments the PET transmission images into a given number of clusters to extract specific areas of differing attenuation such as air, the lungs and soft tissue, preceded by a median filtering procedure. The reconstructed transmission image voxels are therefore segmented into populations of uniform attenuation based on the human anatomy. The clustering procedure starts with an over-specified number of clusters followed by a merging process to group clusters with similar properties and remove some undesired substructures using anatomical knowledge.**

I. Introduction

Attenuation correction in positron emission tomography (PET) represents a key step in the reconstruction process and is now widely accepted by the nuclear medicine community as an essential component of the long chain of modules required for the reconstruction of artefact-free, quantitative data.

Noise from the transmission scan will spread thought the reconstruction process, affecting the quality of the images. To minimize this effect, long transmission scans (10-30 min) are normally acquired to ensure good statistics at the expense of patient comfort especially in the case of whole-body scanning on low-sensitivity partial-ring PET tomographs. During the last decade, techniques based on transmission image segmentation and tissue classification tools have been proposed to minimize the acquisition time (less than 5 min) and increase the accuracy of attenuation correction, while still preserving or even reducing the noise level [1-4]. Segmentation algorithms must reach equilibrium between final image quality and computational time. The majority of them fall into one of the following two groups: thresholding techniques [5, 6] and fuzzy-segmentation techniques [7]. Threshold approaches make use of the gray-level histogram counts to distinguish between regions [8], however, if the histogram is the sole input source, the technique is most likely to fail in regions where the total number of counts is small (e.g. the skull). Their performance strongly depends on the choice of the thresholds.

Fuzzy segmentation techniques on the other side demonstrated excellent performance and produced good results as an automated, unsupervised tool for segmenting noisy images in a robust manner [7, 9, 10]. They are iterative procedures that minimize an objective function. As an output, a membership degree is assigned to every voxel with respect to a cluster centre. Among the algorithms belonging to this class is the Fuzzy-C Means (FCM) clustering algorithm [11, 12]. The number of clusters is normally passed as an input parameter. To automate the process, a cluster validity index can be used to select the optimal number of clusters [13].

The purpose of this work is to develop a powerful and robust segmentation tool, the use of which in combination with morphological information provided by the cluster (sharp boundaries) to improve homogeneity within regions allows to reduce significantly the noise.

II. The Fuzzy C-Means Segmentation Algorithm

For partitioning data sets into groups of similar objects it has been argued that fuzzy approaches work better than crisp ones [11]. This is the case of many iterative algorithms, which converge to a local minimum of the objective function, without any assurance of its proximity to the global minimum. In this situation, a fuzzy clustering method evolves more smoothly to the global minimum whereas a crisp method bears more risk to get stuck in a local minimum. In clustering-based image segmentation, the fuzzy approach is more reliable to crisp one because grey image possesses ambiguity within pixels due to the possible multi-valued levels of brightness in the image [14]. Incertitude in image pattern may be explained in terms of greyness ambiguity. For example, in medical image processing, the fuzzy approach is well suited because biological tissues have overlapping grey-scale

This work was supported by
the Swiss National Science Foundation under grant SNSF 3152-062008.

H. Zaidi, M. Diaz-Gomez and D. Slosman are with the division of nuclear medicine, Geneva University Hospital, Geneva 1211, Switzerland (telephone: +41 22 372 7258, e-mail: habib.zaidi@hcuge.ch).

A. Boudraa is with Ecole Navale, Département Signal, Lanvéoc Poulmic BP600, F 29240 Brest Naval, France.

0-7803-7324-3/02/$17.00 © 2002 IEEE

intensity distributions due to imperfect image uniformity, noise and partial volume effects.

Consider a set of n vectors $X=\{x_1,x_2,\ldots,x_n\}\subset R^p$ to be clustered into $c \in \{1,2,\ldots,n\}$ subsets that represent the structure of X. Each $x_k \in R^p$ is a feature vector consisting of p real-valued measurements (colour, length, …) describing the features of the object represented by x_k. Clustering in unlabeled data X is the assignment of labels to objects generating X. c-partitions of X are sets of $(c\times n)$ values $\{\mu_{ik}\}$ that can be conveniently arranged as a $(c\times n)$ matrix $U=[\mu_{ik}]$. Each element, μ_{ik}, represents the membership degree of x_k to belong to the i^{th} cluster. The set of all $c\times n$ non-degenerate

$$A_{cn} = \Big\{U \in R^{c\times n} \Big| \sum_{i=1}^{c} \mu_{ik} = 1, \sum_{k=1}^{n} \mu_{ik} > 1 \quad and$$
$$\mu_{ik} \in [0,1]; \quad i = 1,\ldots,c; \quad 1 \le k \le n \ \Big\} \subset [0,1]^{c\times n}$$

constrained fuzzy partitions, A_{cn}, is defined as follows:

A well-known model of fuzzy clustering in X is the following objective function [11]:

$$J_m(U,V:X) = \sum_{k=1}^{n}\sum_{i=1}^{c} (\mu_{ik})^m \left\| x_k - v_i \right\|_A^2$$

$U\in A_{cn}$ is a fuzzy partition matrix $m\in[1,+\infty[$ is a weighting exponent called the fuzzifier, $V=(v_1,v_2,\ldots,v_c)$ is a vector of unknown cluster centers (prototypes), $v_i\in R^p$ for $1\le i \le c$ and $\|x\|_A = \sqrt{x^T A x}$ is any inner product norm where A is any positive definite matrix. Good partition U^* of X are taken form (U^*,V^*) that are local minimizers of J_m. The usual method to optimise J_m is to use partial optimisation of U and V. That is, first fix U and find necessary conditions on V to minimize J_m. Then, fix V and minimize J_m with respect to U [11]. Approximate optimisation of J_m by FCM is based on iteration:

$$\mu_{ik} = \left[\sum_{j=1}^{c} \left(\frac{\left\| x_k - v_i \right\|_A}{\left\| x_k - v_j \right\|_A} \right)^{\frac{2}{m-1}} \right]^{-1} \qquad (1)$$

$$v_i = \frac{\sum_{k=1}^{n} \mu_{ik}^m . x_k}{\sum_{k=1}^{n} \mu_{ik}^m} \qquad (2)$$

The FCM algorithm consists of iterations alternating between equations (1) and (2). This algorithm converges to either a local minimum or saddle point of J_m [11]. In this work, feature vector x_k is restricted to the image grey level value l. Thus, in the histogram-based FCM algorithm [10], equations (1) and (2) are formulated as follows:

$$\mu_{il} = \left[\sum_{j=1}^{c} \left(\frac{\left\| l - v_i \right\|_A}{\left\| l - v_j \right\|_A} \right)^{\frac{2}{m-1}} \right]^{-1} \qquad (3)$$

$$v_i = \frac{\sum_{l=0}^{L-1} \mu_{il}^m . H(l) . l}{\sum_{l=0}^{L-1} \mu_{il}^m} \qquad (4)$$

H represents the histogram of image of L-levels, where L is the number of grey levels. Each voxel has a feature that lies in the new discrete set $X=\{0,1,\ldots, L-1\}$. The computation of membership degrees of $H(l)$ voxels is reduced to that of only one voxel with l as grey level value. The histogram-based FCM algorithm is outlined in the following steps:

Step 1) Fix the number of clusters c, $2\le c\le L$ and the threshold value ε;

Step 2) Find the number of occurrences $H(l)$ of l, $l=0,1,..,L-1$;

Step 3) Initialise μ_{il} using the L grey levels such that:

$$\sum_{i=1}^{c} \mu_{il} = 1; \quad l = 0,1,\ldots,L-1$$

Step 4) Compute the centroid according to equation (4)

Step 5) Update the membership degree $\tilde{\mu}_{il}$ according to equation (3)

Step 6) Compute the defect measure

$$E = \sum_{i=1}^{c}\sum_{l=0}^{L-1} \left| \tilde{\mu}_{il} - \mu_{il} \right|$$

Step 7) If $(E>\varepsilon)\{ \mu_{il} \leftarrow \tilde{\mu}_{il}$ goto Step 4$\}$

Step 8) Defuzzification process.

We use as many iterations as required until E is smaller than ε (in our case the threshold was fixed to 0.001). For the defuzzification process, every voxel is assigned to the cluster centre for which it has the maximum membership degree.

III. Attenuation Correction And Image Reconstruction

The ECAT ART tomograph (CTI/Siemens) installed at Geneva University Hospital, was upgraded to use collimated point sources of ^{137}Cs and is capable to produce high quality scatter-free data in this continuously rotating partial-ring tomograph. The images were scatter corrected and reconstructed using normalised attenuation weighted, ordered subset – expectation maximization iterative reconstruction (NAW OSEM) with 2 iterations and 8 subsets [15].

When applying fuzzy clustering algorithms, a common task is to start with an oversized number of clusters. This is done to prevent the fact that the algorithm might misidentify conflicting regions. Some of the problematic regions are the outer boundaries of the lungs and the brain skull. A merging process usually follows this overestimation in order to get to the desired number of clusters according to *a priori* anatomic knowledge. PET transmission images were segmented using the FCM algorithm described above. The algorithm has been largely tested on different data sets, acquired under various timing protocols. Our experiments were valuable to optimise the initial number of clusters (e.g. five in the thorax region).

This overestimation of the actual regions present in the image greatly simplifies the merging process from five clusters to three. From this initial segmentation, the bed is easily identified, and can be removed using a mask filter**.** The filter gives back a binary image, where the soft tissue has one label and the background and lungs share another one. In the final step, the lungs are identified using a labelling technique as outlined in [9, 10]. Bone and soft tissue are considered as a single class since they are indistinguishable on typical short transmission scans.

Fig. 1. Illustration of the segmentation process of the heart/chest phantom transmission images showing from left to right: the original transmission image, FCM segmented image using 5 clusters, merging process to a three-clustered image, and the final attenuation map after applying a Gaussian filter and weighted averaging.

The whole process is illustrated in Fig. 1. Once the transmission image is segmented, the tissue type corresponding to each label is identified (e.g. lungs, soft tissue, air …etc.). The attenuation map is then calculated by weighted averaging combining the segmented and original images using an approach similar to the one described in [5, 6]. To this end, the voxels corresponding to lungs and soft tissue in the original reconstructed transmission images are scaled so that the averages within these regions are μ_{la} and μ_{sa}, respectively. The voxels within these regions are then filtered to reduce statistical noise and scaled to the expected attenuation density value. The hybrid attenuation map $f_h(x,y)$ is then calculated as follows:

$$f_h(x,y)=\begin{cases} w_s\mu_{sFCM}+\dfrac{\mu_{st}}{\mu_{sa}}f_s(x,y)\times(1-w_s) & \text{if } (x,y)\in \text{soft tissue region} \\ w_l\mu_{lFCM}+\dfrac{\mu_{lt}}{\mu_{la}}f_l(x,y)\times(1-w_l) & \text{if } (x,y)\in \text{lung region} \\ \mu_a=0 & \text{if } (x,y)\in \text{air region} \end{cases} \quad (5)$$

where μ_{st}, μ_{lt} , μ_{sa}, μ_{la} are the theoretical and average attenuation coefficients (obtained from the transmission image) for soft tissue and lung tissue, respectively. μ_{sFCM} and μ_{lFCM} are attenuation coefficients corresponding to the cluster centres of the segmented transmission image. The attenuation coefficient for air μ_a was neglected. The class-dependent weighting factors w_s and w_l control to what degree the true values are emphasized [1] and were identical to the values reported in [6].

Subsequently, a high statistics transmission bed scan was acquired and the images processed using the same reconstruction and processing protocol. This low noise image of the bed is added up to the final segmented transmission images. The code was implemented to account for the different bed elevations between the bed scan and the clinical data sets by reading the appropriate information from the header of both images. The boundaries are then made more natural by applying a 5*x*5 Gaussian filter.

The proposed fuzzy clustering-based segmented attenuation correction (FCSAC) scheme was compared to both the standard measured attenuation correction (MAC) [16] applied in clinical routine in our division and histogram thresholding-based segmented attenuation correction (TSAC) based on ref. [5, 6]. The original transmission images were segmented using both the FCM and thresholding techniques, respectively. The attenuation correction matrix is then calculated by forward projection at appropriate angles of the resulting processed transmission image. The generated ACFs map was then used to reconstruct the emission data.

IV. Phantom And Clinical Studies

A. Phantom studies

Both the anthropomorphic Rando Alderson and chest/heart phantoms were used to assess qualitatively and quantitatively the performance of the FCM segmentation algorithm. Transmission scans of 2, 3, 5 and 10 minutes were acquired at the chest region. Transmission images were then segmented and compared with the original reconstructed images after full processing. The chest phantom simulates the lungs, heart cavity and the spine. The heart cavity compartments were filled with different concentrations of a Ge-68 dissolution chosen to mimic the activity concentration generally encountered in clinical practice. The activity of each compartment was carefully calibrated using a well counter. A total 76 ROIs were drawn in the different compartments of the heart phantom and background for each image, and the activity concentration within each ROI determined.

B. Clinical studies

The attenuation correction schemes were also tested on 22 oncology patients referred to the division of nuclear medicine of Geneva University Hospital. For the quantitative analysis, we investigated any significant differences in the standard uptake values (SUV) when using different protocols during the processing of the transmission scans. With the advise of an experienced physician, manual ROIs were drawn on the clinical studies that were diagnosed with lung cancer. We then calculated maximum and average SUV values and sets of linear regression plots were drawn between different processing techniques.

V. Results

Fig. 2 illustrates the performance of the segmentation algorithm on a short transmission scan of the Alderson anthropomorphic phantom. It can be clearly seen that the segmentation algorithm performs well even with short acquisition times on this low-sensitivity scanner (approximately 1/3 of the equivalent full-ring scanner, the ECAT EXACT). The contours of the lungs are well defined and the outer boundaries clearly and accurately delineated.

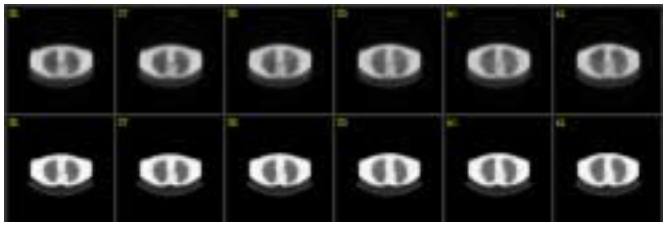

Fig. 2. Illustration of the performance of the segmentation algorithm on the Alderson anthropomorphic phantom (2 min acquisition time). From top to bottom, unprocessed transmission images followed by FCM segmented attenuation map.

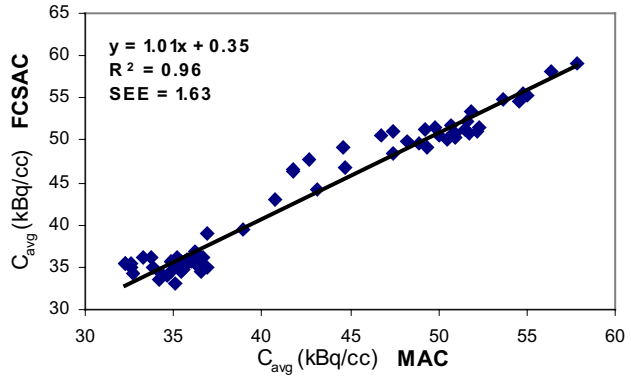

Fig. 3. Correlation plots between heart phantom's average concentrations (C_{avg}) when using MAC and FCSAC. Correlation coefficients, best-fit equations and standard error of estimates are also included.

Fig. 3 shows results of a linear regression plot illustrating correlation between MAC and FCSAC. The line connecting the data points represents the result of a linear regression analysis. There is very good correlation (r=0.96) between MAC and FCSAC and the regression line agreed well with the line of identity (slope=1.01). The dispersion of data points is insignificant and the general trend as shown by the regression line is that the coefficients of variations are similar. However, TSAC leads to 3.5% lower overall estimates than MAC, whereas FCSAC leads to 1% higher estimates. An excellent correlation was also obtained between TSAC and FCSAC as well as MAC and TSAC. The percent differences between the correction techniques are minor but statistically significant ($p<0.01$).

3.2. *Clinical studies*

A representative slice of a clinical study at the level of the thorax is shown in Fig. 4 illustrating the original reconstructed and segmented images after the labelling process and finally after assigning the tissue-dependent attenuation coefficients using weighted averaging. The improvement in image quality of emission data reconstructions when using FCSAC as compared to MAC is further illustrated on coronal slices of a patient study in Fig. 5. The images are less noisy and show more uniform uptake of the tracer. In our clinic, measured attenuation correction is applied routinely but the physicians preferred the images obtained with FCM-based segmented attenuation correction and judged image quality to be much superior.

Fig. 4. Illustration of the FCM segmentation algorithm on a clinical study at the thorax level showing from left to right: the reconstructed transmission image, the corresponding segmented image, and the final attenuation map.

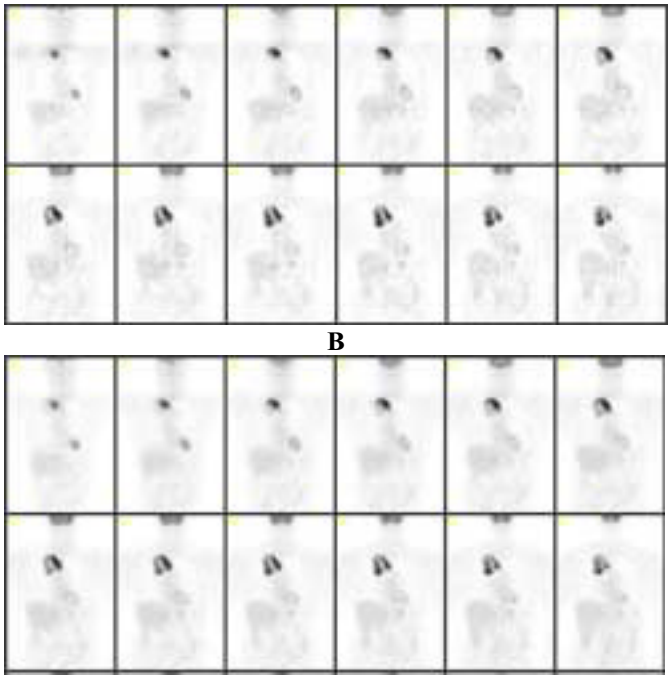

Fig. 5. Illustration of the improvement in image quality when using segmented attenuation correction. **A.** Reconstructions using measured attenuation correction. **B.** Reconstructions using fuzzy clustering-based segmented attenuation correction.

Fig. 6 shows the correlation between SUV estimates when using MAC and FCSAC. The line connecting the data points represents the results of a linear regression analysis. The results of the statistical analysis of the patient SUV data are summarised in table 1. These results confirm the existence of a statistically significant difference between the different techniques, except MAC and FCSAC where no proof of statistically significant differences on the average SUVs was observed (P=0.27, paired t-test). There was a very good correlation (R^2=0.96) between maximum SUVs in lung nodules measured on images reconstructed with measured and segmented attenuation correction with a statistically significant decrease in SUV_{max} (17.0%±8.4%, P<0.01) on the latter images. According to these data, the noise in MAC appears to be 19% higher overall than both TSAC and FCSAC.

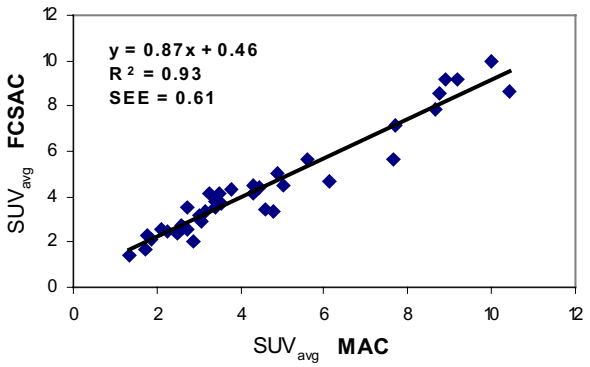

Fig. 6. Correlation plots between patients' average SUV estimates obtained using MAC and FCSAC.

TABLE I
SUMMARY OF STATISTICAL COMPARISON BETWEEN CLINICAL AVERAGE AND MAXIMUM SUV DATA ESTIMATED USING THE USUAL MAC, TSAC AND FCSAC PROTOCOLS. THE AVERAGE PERCENT DIFFERENCES AND ASSOCIATED STATISTICAL DIFFERENCE ARE SHOWN.

Attenuation correction methods	SUV_{avg}		SUV_{max}	
	% Diff.	Prob.	% Diff.	Prob.
MAC / TSAC	12.0±7.9	<0.01	17.0±8.4	<0.01
MAC / FCSAC	11.1±10.1	>>0.20	12.8±12.6	<0.01
TSAC / FCSAC	12.3±7.5	<0.01	11.8±8.0	<0.01

VI. DISCUSSION AND CONCLUSIONS

The quantitative capability of PET measurements depends strongly on the accuracy of attenuation and scatter corrections. While scatter correction in whole-body PET imaging is only approximate and has limited accuracy [17], attenuation correction is exact and is limited mainly by the statistics of the acquired data. In a clinical environment, the most accurate attenuation correction techniques are based on measured transmission data acquired before (pre-injection), during (simultaneous), or after (post-injection) the emission scan. More refined transmission image segmentation and tissue classification tools were also proposed to increase the accuracy of attenuation correction when using short transmission scanning times [6, 18]. Once the attenuation map is obtained, the correction matrix is calculated by forward projection at appropriate angles of the resulting processed transmission image.

A number of factors influence the accuracy of attenuation correction in PET imaging when one uses histogram-based threshold edge detection methods. As stated by many authors, no single threshold is ideal for all object shapes and sizes and each group picked the threshold that best matched their specific phantom or clinical studies, transmission source type and imaging system [8]. Other interesting approaches to segment noisy transmission data include the use of active contour models [19], neural networks [4], morphological segmentation [3] and hidden Markov modelling [1]. The addition of fuzzy clustering-based segmentation to the attenuation correction process in ^{18}F-FDG PET markedly improves image quality and lesion-to-background contrast. This resulted in an improved lesion detection rate in patients with lung cancer, diagnostic performance and more accurate staging. Fuzzy clustering-based segmented attenuation correction in PET shows a clear reduction of noise propagation from transmission into emission data, allowing for reduction of transmission scan duration.

VII. REFERENCES

[1] J. M. M. Anderson, B. A. Mair, and M. Rao, "Attenuation correction for PET using a hidden Markov model based segmentation method.," presented at *Proc.* IEEE Nuclear Science Symposium and Medical Imaging Conference, 1999.

[2] B. Reutte, G. J. Klein, and R. H. Huesman, "Automated 3-D segmentation of respiratory-gated PET transmission images.," *IEEE Trans Nucl Sci*, vol. 44, pp. 2473-2476, 1997.

[3] C. Riddell, P. Brigger, R. E. Carson, and S. L. Bacharach, "The watershed algorithm: a method to segment noisy PET transmission images.," *IEEE Trans Nucl Sci*, vol. 46, pp. 713 -719, 1999.

[4] S. K. Yu and C. Nahmias, "Segmented attenuation correction using artificial neural networks in positron tomography.," *Phys Med Biol*, vol. 41, pp. 2189-2206, 1996.

[5] M. Xu, W. K. Luk, P. D. Cutler, and W. M. Digby, "Local threshold for segmented attenuation correction of PET imaging of the thorax.," *IEEE Trans Nucl Sci*, vol. 41, pp. 1532 -1537, 1994.

[6] M. Xu, P. Cutler, and W. Luk, "An adaptive local threshold segmented attenuation correction method for whole-body PET imaging.," *IEEE Trans Nucl Sci*, vol. 43, pp. 331-336, 1996.

[7] V. Bettinardi, E. Pagani, M. C. Gilardi, C. Landoni, C. Riddell, G. Rizzo, I. Castiglioni, D. Belluzzo, G. Lucignani, S. Schubert, and F. Fazio, "An automatic classification technique for attenuation correction in positron emission tomography.," *Eur J Nucl Med*, vol. 26, pp. 447-458, 1999.

[8] K. Bilger, J. Kupferschlager, W. Muller-Schauenburg, F. Nusslin, and R. Bares, "Threshold calculation for segmented attenuation correction in PET with histogram fitting.," *IEEE Trans Nucl Sci*, vol. 48, pp. 43-50, 2001.

[9] A. E. Boudraa, J. Champier, L. Cinotti, J. C. Bordet, F. Lavenne, and J. J. Mallet, "Delineation and quantitation of brain lesions by fuzzy clustering in positron emission tomography.," *Comput Med Imaging Graph*, vol. 20, pp. 31-41, 1996.

[10] A. O. Boudraa, S. M. Dehak, Y. M. Zhu, C. Pachai, Y. G. Bao, and J. Grimaud, "Automated segmentation of multiple sclerosis lesions in multispectral MR imaging using fuzzy clustering.," *Comput Biol Med*, vol. 30, pp. 23-40, 2000.

[11] J. C. Bezdek, *Fuzzy mathematics in pattern classification.*, Cornell Univ. Ithaca ed. New York: The Institute of Electrical and Electronics Engineers, Inc., 1973.

[12] J. C. Bezdek, R. J. Hathaway, M. J. Sabin, and W. T. Tucker, "Convergence theory for fuzzy c-means: counterexamples and repairs.," *IEEE Trans Syst Man Cybern*, vol. 17, pp. 873-877, 1987.

[13] N. R. Pal and J. C. Bezdek, "On cluster validity for the fuzzy c-means model.," *IEEE Trans Fuzzy Syst*, vol. 3, pp. 370-379, 1995.

[14] N. R. Pal and S. K. Pal, "A review on image segmentation techniques.," *Pattern Recognition*, vol. 25, pp. 1277-1294, 1993.

[15] C. Michel, M. Sibomana, A. Boi, X. Bernard, M. Lonneux, M. Defrise, C. Comtat, P. E. Kinahan, and D. W. Townsend, "Preserving Poisson characteristics of PET data with weighted OSEM reconstruction.," presented at *Proc.* IEEE Nucl Sci Symp & Med Imag Conf, 1998.

[16] C. C. Watson, A. Schaefer, W. K. Luk, and C. M. Kirsch, "Clinical evaluation of single-photon attenuation correction for 3D whole-body PET.," *IEEE Trans Nucl Sci*, vol. 46, pp. 1024 -1031, 1999.

[17] H. Zaidi, "Scatter modelling and correction strategies in fully 3D PET.," *Nucl Med Comm*, vol. 22, pp. 1181-1184, 2001.

[18] S. R. Meikle, M. Dahlbom, and S. R. Cherry, "Attenuation correction using count-limited transmission data in positron emission tomography.," *J Nucl Med*, vol. 34, pp. 143-150, 1993.

[19] Y.-C. Tai, K.-P. Lin, M. Dahlbom, and E. J. Hoffman, "A hybrid attenuation correction technique to compensate for lung density in 3-D total body PET.," *IEEE Trans Nucl Sci*, vol. 43, pp. 323 -330, 1996.